Electronic Supplementary Material (ESI) for Energy & Environmental Science

Supporting Information

Low-Temperature Processed Mesosuperstructured to Thin-Film Perovskite Solar Cells

James M. Ball,[1] Michael M. Lee,[1] Andrew Hey,[1] and Henry J. Snaith[1]

[1]Department of Physics, University of Oxford, Clarendon Laboratory, Parks Road, Oxford, OX1 3PU, UK

1. Methods and Materials

Device Fabrication

The synthesis of the perovskite, $CH_3NH_3PbI_{3-x}Cl_x$, has been reported elsewhere.[1] All processing was performed in air. Devices were fabricated on fluorine doped tin oxide (FTO) coated glass substrates. The substrates were cleaned sequentially in hallmanex, acetone, isopropanol and O_2 plasma. A compact layer of TiO_2 was subsequently deposited by spin-coating a mildly acidic solution of titanium isopropoxide in ethanol, and heated at 500°C for 30 minutes. The low-temperature mesostructured scaffold was deposited by spin-coating (speed = 2500 rpm, ramp = 2500 rpm/s, time = 60s) a colloidal dispersion of < 50 nm Al_2O_3 nanoparticles (Sigma-Aldrich, product number 702129) in isopropanol, followed by drying at 150°C for 1 hour. The high-temperature mesostructured scaffold was deposited by spin-coating a colloidal dispersion of < 50 nm Al_2O_3 nanoparticles and cellulose in a mixture of butoxyethanol and ethanol, followed by sintering at 500°C for 30 minutes. The final thickness of the scaffold was controlled by varying the initial concentration of nanoparticles in dispersion before spin-coating. Upon cooling to room temperature, the perovskite was deposited by spin-coating (speed = 2000 rpm, ramp = 2000 rpm/s, time = 60s) from a ~40 wt% DMF solution of methylammonium iodide and $PbCl_2$ (3:1 molar ratio) which formed the perovskite after heating to 100°C for 45 minutes. The hole-transport layer was deposited by spin-coating an 11 vol. % 2,2′,7,7′-tetrakis-(*N*,*N*-di-*p*-methoxyphenylamine)9,9′-spirobifluorene (spiro-OMeTAD) in chlorobenzene solution with added tert-butylpyridine (tBP) and lithium bis(trifluoromethanesulfonyl)imide (Li-TFSI). Finally, devices were completed with evaporation of Ag contact electrodes through a shadow mask.

Device Characterisation

Current-voltage characteristics were measured under AM 1.5 100 $mWcm^2$ simulated sunlight (ABET Technologies Sun 2000) with a Keithley 2400. The apparatus for device characterization was calibrated with an NREL certified KG5 filtered Si reference diode. The cell area under test was defined with a square aperture in a metal mask [2] to be approximately 0.09 cm^2.

The light-harvesting efficiency (LHE) was calculated by measuring the light absorption in complete devices using an integrating sphere to account for optical losses outside of the active layer. The experimental details are published in depth elsewhere [3]. In brief, following calibration and correction with a silver mirror, the reflectance (R) from a device mounted on an 8° wedge at the exit port of the integrating sphere was measured. In the complete device, incident light makes two passes through the active layer so the proportion of collected light is that which is not absorbed in the device i.e. $R = 1 – A_{device}$, where A_{device} is the absorption of the solar cell. We neglect the small fraction of light absorbed in the Ag electrode. However, the significant light absorption in the FTO (A_{FTO}) does not contribute to the photocurrent and should be accounted for when estimating the light-harvesting efficiency of the active layer. To make an approximation for the light absorbed in the FTO, we have simply assumed two passes of light and neglected multiple reflections and coherence. Accounting for absorption in the FTO over two passes of light and allowing for the attenuation of the light intensity having passed through the active layer, the light-harvesting efficiency of the active layer is given by equation 1.

$$LHE = 1 - \frac{R}{1 - A_{FTO}} - A_{FTO} \qquad (1)$$

A_{FTO} is measured with the integrating sphere using clean FTO glass, without a silver back-reflector, using a combination of reflectance and transmittance (T) measurements, where $A = 1 − T − R$.

Perovskite and Al_2O_3 Scaffold Characterization

Unless otherwise stated, sample thicknesses were measured using a Veeco Dektak 150 surface profilometer. Where quoted, mean thicknesses were calculated based on 5 measurements. Scanning electron microscopy (SEM) images were obtained using a Hitachi S-4300.

X-ray diffraction (XRD) spectra were obtained from samples of perovskite coated on Al_2O_3 scaffolds on glass microscope slides using a Panalytical X’Pert Pro x-ray diffractometer.

The amount of dye desorbed from a mesosuperstructured scaffold was used as a representative metric for its surface area. After sintering, the Al_2O_3 scaffolds were cooled to ~70°C and then immersed into a 10 mM solution of N719 dye in acetonitrile:tert-butanol (volume ratio of 1:1) for 18 hours. The substrates were then rinsed in the acetonitrile, dried, and then rinsed in an aqueous 200 mM KOH solution to remove the dye. The number of dye molecules on the surface was measured by taking the absorption spectrum of the dye/KOH solutions, assuming the visible peak molar extinction coefficient of N719 to be

14700 $M^{-1}cm^{-1}$ [4]. A complementary measurement of the scaffold area and thickness allows a determination of the number of dye molecules desorbed per unit volume of scaffold.

2. Supplementary Discussion

Al_2O_3 SEM

We initially investigated the properties of the scaffold fabricated at low-temperature. Planar SEM images shown in Figure S1 qualitatively indicate that, indeed, the films are porous. Varying the processing conditions investigated in the present work appears to produce indistinguishable films as observed with SEM.

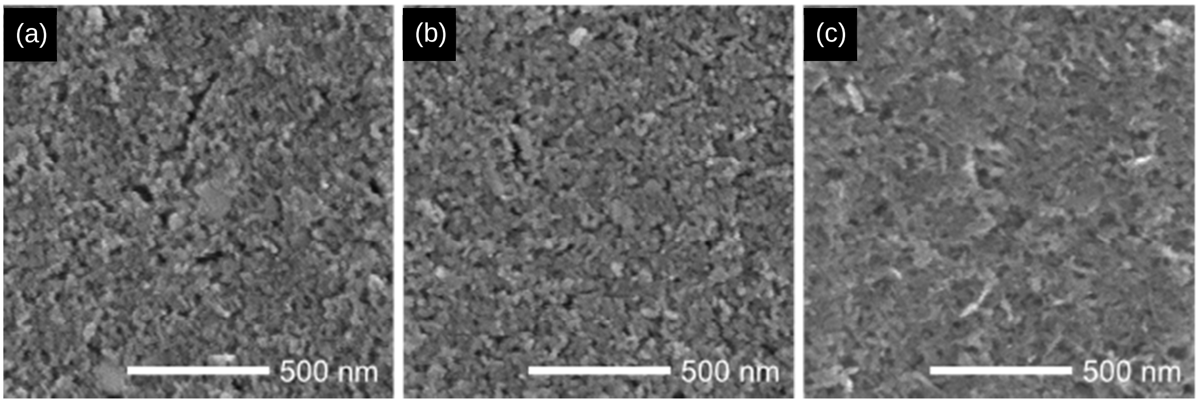

Figure S1. Planar SEM images of (a) low-temperature sintered Al_2O_3 from a dispersion without polymer binder, (b) high-temperature sintered Al_2O_3 from a dispersion without polymer binder, and (c) high-temperature sintered Al_2O_3 from a dispersion with polymer binder.

Al_2O_3 Scaffold Surface area

Based on dye desorption from the scaffold, the number of dye molecules per volume of scaffold was found to be 1.7×10^{20} cm^{-3} and 3.1×10^{20} cm^{-3} from the low-temperature paste and the control high-temperature paste including binder, respectively. Given the dye must be confined to the surface of the particles prior to desorption, this suggests the free surface area of the low-temperature sintered films is approximately half of that of a high-temperature sintered film initially incorporating a polymer binder.

Perovskite Capping Layer Thickness

The thickness of the perovskite capping which forms on top of the alumina scaffold was measured as a function of scaffold thickness as shown in Figure S2. The data suggests that the capping layer only forms for a scaffold thinner than ~400 nm.

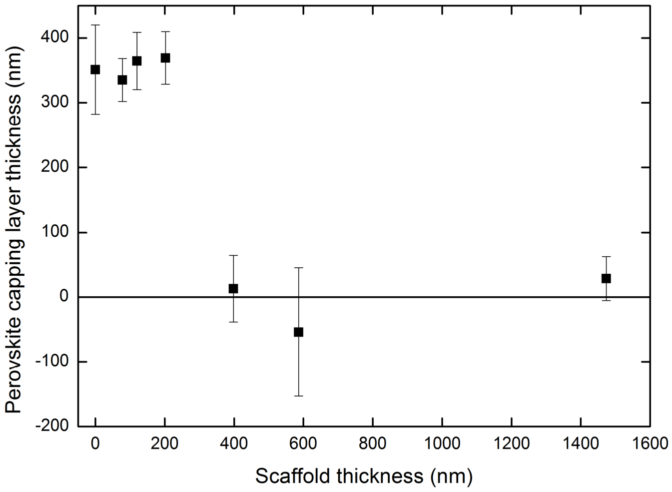

Figure S2. Perovskite capping layer thickness as a function of scaffold thickness.

X-Ray Diffraction of Perovskite Layers

X-ray diffraction measurements from the perovskite were used to assess any changes to the crystal size as a function of scaffold thickness. Normalized XRD spectra are shown in Figure S3a. The peak positions are in agreement with the previous report of the same perovskite [1].

The average crystallite size can be estimated from the full-width at half maximum (FWHM) of the most intense peak using the Scherrer equation.[5] For the ~80 nm and 0 nm scaffolds, the peak widths were at the limit of machine broadening so the crystallite size could not be calculated. Accounting for machine broadening, Figure S3b shows the crystallite size as a function of scaffold thickness. We note that this method of calculating the crystallite size is sensitive to small changes at large crystal sizes. However, the variation is systemic and therefore qualitatively demonstrates a trend. The crystallite size is found to decrease with increasing scaffold thickness. For thin scaffolds, the XRD spectrum contains the contribution of perovskite within the pores, in addition to the capping layer. It is possible that the crystallite size within the pores is confined by the pore volume. As the scaffold thickness increases, the relative portion of perovskite in the pores increases and therefore the average crystallite size decreases. For thickness' greater than 400 nm, the crystallite size begins to saturate. This may be expected when the perovskite no longer fills the pore volume but rather coats the internal surface.

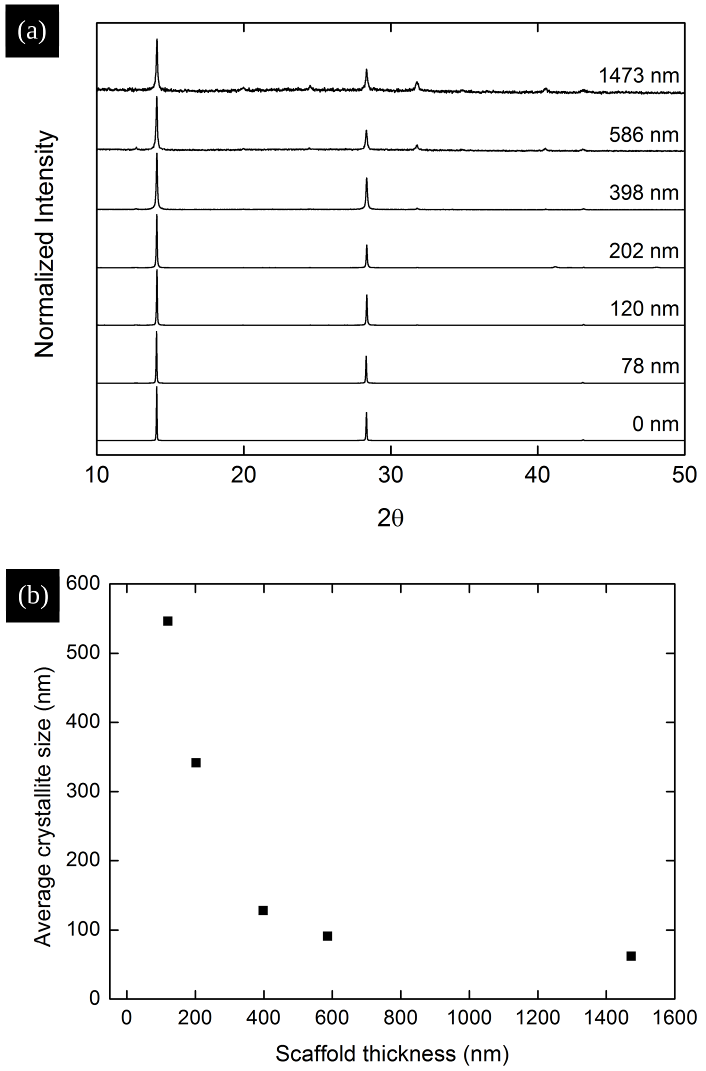

Figure S3. (a) Normalized XRD spectra for different scaffold thicknesses as indicated. (b) Lower estimate for the crystallite size based on the Scherrer equation.

Device Characteristics

The current-voltage characteristics of the most efficient device for a device without a scaffold (4.9%), the most efficient device with a perovskite capping layer (9.1%) and the most efficient device with a very thick scaffold (5.3%) from a single batch of devices are presented in Figure S4. All the device parameters from the batch are shown in the box and whisker plots in Figure S5. The box edges are the standard error, the whiskers are the maximum and minimum of the distributions and the centre horizontal line is the median. The data from the distributions are shown adjacent to the box plots.

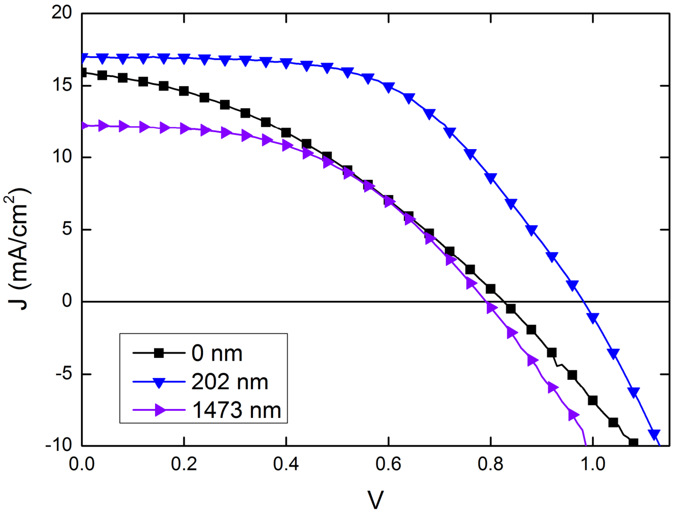

Figure S4. Current-voltage characteristics of most efficient device for a device without a scaffold (4.9%), the most efficient device with a perovskite capping layer (9.1%) and the most efficient device with a very thick scaffold (5.3%) from a single batch of devices.

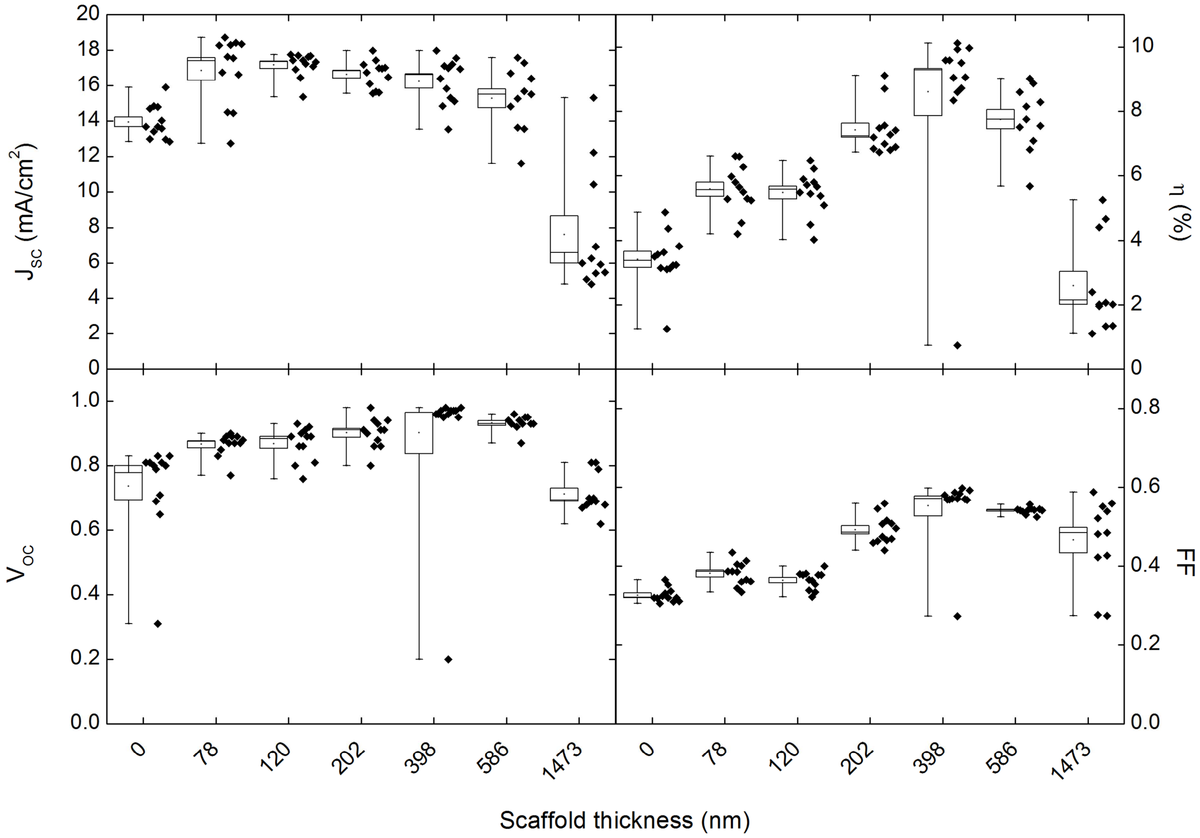

Figure S5. Box and whisker plots for all the device parameters from the batch described in the text. Data are shown adjacent to the boxes.

Active Layer Light-Harvesting Efficiency

The variation in short-circuit current (J_{sc}) with scaffold thickness can be due to variations in the amount of light absorbed by the active layer, the charge-collection efficiency (η_{cc}) and the charge-separation efficiency (η_{sep}). The internal quantum efficiency (IQE) is given by IQE = $\eta_{cc} \cdot \eta_{sep}$. To account for variation in the light absorption in the active layer as a function of scaffold thickness, the LHE (proportion of light incident on the cell which gets absorbed by the active layer) was measured. The LHE spectra of the active layer measured on complete devices incorporating a low-temperature sintered Al_2O_3 scaffold are shown in Figure S6a.

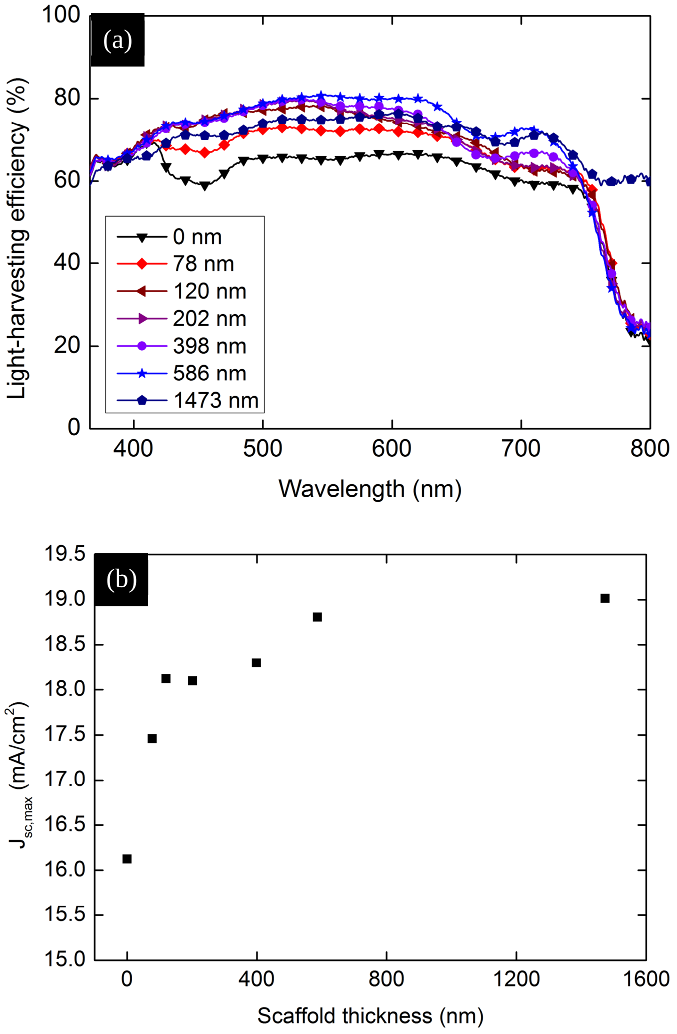

Figure S6. (a) Light-harvesting efficiency of complete devices incorporating a low-temperature sintered Al2O3 scaffold. Spectra are shown for different thicknesses of scaffold as indicated in the legend. (b) Maximum attainable Jsc given the LHE spectra in (a).

The J_{sc} in terms of LHE and IQE is given by equation 2 where P_{in} is the incident solar irradiation at AM 1.5, E_λ is the energy of an incident photon and q is the charge of an electron.

$$J_{sc} = q\int_{\lambda_{\min}}^{\lambda_{\max}} LHE \cdot IQE \cdot \frac{P_{in}}{E_\lambda} d\lambda \qquad (2)$$

The maximum attainable photocurrents based on the LHE spectra (assuming all absorbed photons create separated charges that get collected) are given in Figure S6b. This shows the opposite trend with scaffold thickness to the measured J_{sc}. We therefore conclude that the decrease in measured Jsc with increasing scaffold thickness is due to a decrease in IQE. Based on the LHE spectra and Jsc from device measurements, the IQE integrated of the absorption spectrum can be estimated from equation 2. This is shown in Figure 3b in the main text.

In the absence of optical losses, a solar cell with an absorber band gap of 1.55 eV with 100% quantum efficiency would generate a short-circuit current of 27.53 mA/cm^2. In our cells, there are optical losses. If all the sunlight below the bandgap of the perovskite which gets reflected or absorbed by the FTO glass substrate (see Figure 3) were converted to current, it would account for 3.07 and 3.25 mA/cm^2, respectively. In addition, the calibration of the integrating sphere only accounts for wavelengths down to 366 nm. If all the sunlight below this wavelength is converted to current, it accounts for 0.63 mA/cm^2. For the example device spectrum in Figure 3, the light which is not absorbed or reflected by the cell (green region) accounts for 2.28 mA/cm^2 assuming 100% quantum efficiency.

Device Reproducibility

The device parameters shown in Figure 2 indicate the mean and standard deviation of measurements from 12 unique devices made under the same conditions. A histogram of 78 power conversion efficiencies, each corresponding to a unique device of the most efficient architecture used in the present report, is shown in Figure S7.

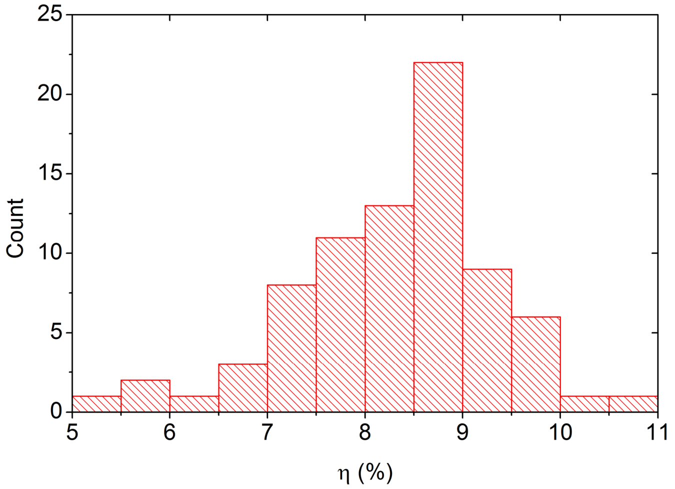

Figure S7. Histogram of device efficiencies from 78 unique devices fabricated with a ~400 nm alumina scaffold, the most efficient device architecture explored in the present report.

High-temperature Processed Al_2O_3 with polymer binder

Control devices using an Al_2O_3 scaffold processed from a paste containing polymer binder and sintered at 500°C were also fabricated. The current-voltage characteristics of the most efficient device from a batch of 91 cells with a scaffold thickness in the range 100–350 nm are shown in Figure S8. A histogram of efficiencies from this batch is shown in Figure S9. The average efficiency from this batch is greater than that previously reported for the same perovskite.

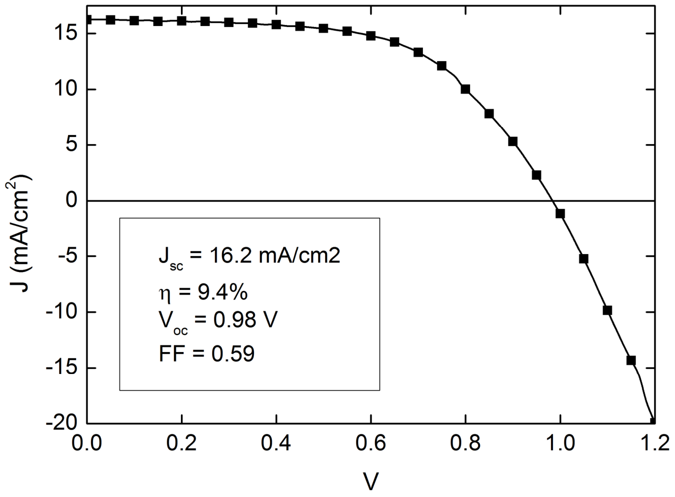

Figure S8. The current-voltage characteristics of the most efficient device from a batch of 91 cells with a scaffold thickness in the range 100–350 nm.

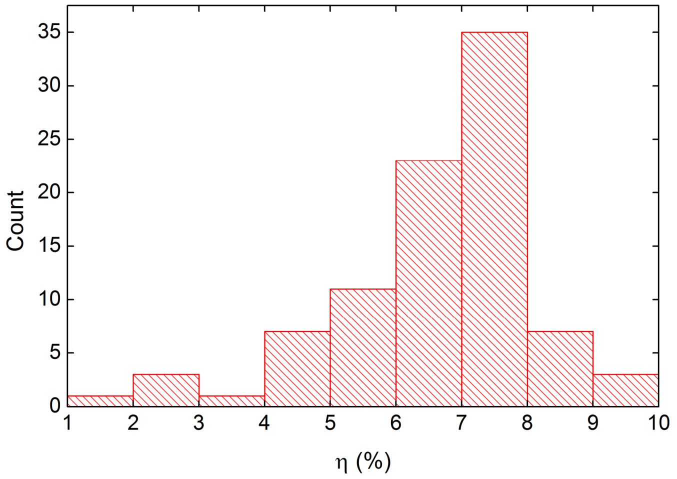

Figure S9. A histogram of efficiencies from a batch of 91 cells.

References

1. M. M. Lee, J. Teuscher, T. Miyasaka, T. N. Murakami and H. J. Snaith, *Science*, 2012, **338**, 643-647.
2. H. J. Snaith, *Energy Environ. Sci.*, 2012, **5**, 6513-6520.
3. H. J. Snaith and C. Ducati, *Nano Lett.*, 2010, **10**, 1259-1265.
4. P. Wang, C. Klein, R. Humphry-Baker, S. M. Zakeeruddin and M. Grätzel, *J. Am. Chem. Soc.*, 2004, **127**, 808-809.
5. A. L. Patterson, *Physical Review*, 1939, **56**, 978-982.